Computers and Geotechnics 38 (2011) 905–916

Contents lists available at ScienceDirect

Computers and Geotechnics

journal homepage: www.elsevier.com/locate/compgeo

Investigation of the cracking of CFRD face plates

Yalin Arici *

Dept. of Civil Engineering, Structural Mechanics Laboratory, K2-303, Middle East Technical University, 06531, Turkey

ARTICLE INFO

Article history:
Received 12 November 2010
Received in revised form 11 June 2011
Accepted 13 June 2011
Available online 22 July 2011

Keywords:
CFRD
Earthquake
Interface
Crack width
Creep
Long-term deformation

ABSTRACT

The primary goal of this study was to examine the cracking behavior of the face plate of a CFRD over its life cycle. Analyses of the construction stage, impounding, long-term deformation and earthquake loading were conducted in sequential phases using a 2-D plane-strain model with the appropriate nonlinear constitutive relationships for the dam constituents. The state of stress and the cracking behavior of the plate were found to be substantially different in the short and long term. Earthquake loading appears to be a critical load condition for the face plate; cracking increased significantly after ground shaking.

1. Introduction

Concrete faced rockfill dams (CFRDs) are very popular in developing countries, as they can be constructed rapidly and easily compared to clay core earthfill dams. Structural and geotechnical designs of such systems are based on precedence, with little emphasis on modern analysis techniques. Empirical formulas are generally used to estimate the crest settlement and the face plate thickness for design purposes. Recent experiences in a major dam project [1] raised questions about this common approach and underlined the importance of conducting more field and laboratory research of CFRDs, especially to develop analytical approaches in predicting the complex behavior of these systems using advanced constitutive models.

The significance of using advanced constitutive models in the simulation of dam behavior was demonstrated in [2], where a substantial improvement in the deformation prediction for a rockfill dam was obtained using a work hardening/softening elasto-plastic model instead of a simple elastic–perfectly plastic (Mohr–Coulomb) model. Using a similar calibration process, reasonable displacement predictions were obtained for the construction stage of a dam by using a fully coupled flow-stress analysis [3]. The hysteretic behavior of soils under slow or rapid cyclic loading can also be simulated with plasticity models. An elasto-plastic constitutive model was compared to a critical-state-type model employing a kinematic yield surface to predict the effects of drawdown-impounding cycles on a dam [4]. Multi-surface plasticity models with kinematic hardening [5–8], simulating the behavior of soils under cyclic loading conditions, were also successfully employed in advanced simulations of embankments [9,10].

There have been several numerical studies on CFRDs focusing on performance during seismic loading [11–13]. Using a linear elastic model for the concrete face plate, axial tensile stresses of up to 20 MPa were obtained during earthquake excitation on a face plate in [11]. The nonlinear, confinement–dependent behavior of rockfill and the stick slip behavior of the interface were modeled in [12]; compressive and tensile stresses as high as 6 and 4 MPa, respectively, were obtained during shaking. Considering the effect of the reservoir, principal tensile stresses on the order of 5 MPa were obtained for the face plate in [13]. A face plate, as described in these studies, can be subjected to high tensile stress, necessitating detailed nonlinear modeling for an accurate prediction of its performance.

The primary purpose of this paper was to investigate the nonlinear behavior of the face plate of a CFRD during impounding, long-term deformation and earthquake loading. A total strain-based crack model with embedded reinforcements was used to predict crack development in the face plate. To model the rockfill behavior during the impounding and construction stages, a plasticity model that incorporated nonlinear elasticity was used. Time-dependent deformation after the impounding was simulated using a visco-elastic model assuming a constant reservoir level during the operating period. A modified Ramberg–Osgood model that incorporated confinement–dependent degradation and damping

* Tel.: +90 312 2107477; fax: +90 312 2107991.
E-mail address: yarici@metu.edu.tr

0266-352X/$ - see front matter © 2011 Elsevier Ltd. All rights reserved.
doi:10.1016/j.compgeo.2011.06.004

Nomenclature

a	parameter determining reference shear strain for Ramberg–Osgood model
b	parameter determining reference shear strain for Ramberg–Osgood model
A	equivalent area encasing a single bar
$\overline{\mathbf{C}}$	six by six dimensionless matrix used in creep formulation
d_c	clear cover distance
E	Young's modulus
E_i	Young's modulus for the ith Kelvin chain in creep model
$\tilde{E}(t)$	tangential Young's modulus for the creep model
f_c	concrete peak compressive strength
f_t	concrete peak tensile strength
f_y	steel yield stress
G_b	shear modulus at the base of the dam
G_f^I	concrete fracture energy
G_{ref}	reference shear modulus
h	concrete effective element size
$J(t,s)$	creep function
$\dot{\lambda}$	interface element internal parameter
K_{ref}	reference compression modulus
m	material parameter for nonlinear elasticity
p'	effective mean stress
$\mathbf{R}$	6×6 factor matrix used in rockfill plasticity formulation
p_a	atmospheric pressure
p'_t	compression offset used in nonlinear elasticity for rockfill constitutive model
p_c	preconsolidation pressure
q'	effective deviatoric stress
t_n, t_t	normal and tangential tractions for the interface elements
$w_{\max}$	crack width
α	Ramberg–Osgood model backbone parameter
β	Ramberg–Osgood model backbone parameter
β_1	internal parameter for rockfill plasticity model
β_{GL}	strain gradient factor for Gergely–Lutz formula
$\Delta p'$	pressure shift for the shear yield surface in rockfill plasticity model
$\Delta\boldsymbol{\gamma}^p$	equivalent plastic strain increment
Δ_y	crest settlement
$\boldsymbol{\varepsilon}$	strain tensor
ε_v^e	elastic volumetric strain
ε_v^p	plastic volumetric strain
ε_v	volumetric strain
ε_y	steel yield strain
ε_{scr}	reinforcement strain
ϕ	friction angle
ϕ_I	friction angle of the interface
ϕ_{cv}	friction angle at constant volume for rockfill plasticity model
$\boldsymbol{\gamma}$	deviatoric strain vector
γ_{xy}	shear strain in x–y plane
γ_r	reference shear strain value
η_1	viscosity of the damper used in creep model
κ_1	internal model variable for tracking of hardening behavior of shear failure surface
κ_2	internal model variable for tracking of hardening behavior of compression cap
λ_1	retardation time in creep model
$\dot{\lambda}$	interface element internal model parameter
λ_i	retardation time for the i^{th} Kelvin chain in creep model
θ	Lode's angle
ϑ	dilation angle for rockfill
ϑ_I	dilation angle for the interface
$\dot{\boldsymbol{\sigma}}$	stress rate tensor
$\boldsymbol{\sigma}$	stress tensor
σ'_1	confinement stress for rockfill triaxial tests
υ	poisson ratio
$\xi_{\max}$	maximum damping value for Ramberg–Osgood model

properties was used as the constitutive relationship for the rockfill material during seismic loading. The rockfill-face plate interface was modeled using a plasticity model that can simulate gap opening, sliding and dilation. Using a 2D plane-strain model with the appropriate constitutive laws for each period of a dam's life cycle, this study was conducted to investigate the following: (1) the importance of modeling the construction stages and impounding to understand face plate behavior, (2) the effect of the interface and the stress transfer mechanism on the formation of plate stress, (3) the effect of long-term settlement of the fill on plate performance and (4) the performance of the face plate during a moderate seismic event.

There are some limitations to this study. First of all, the deformations of the face plate parallel to the dam axis or the opening of the vertical construction joints cannot be predicted within the scope of this work as such an investigation would require a 3D model of the system. The study is also limited to a numerical prediction of the dam behavior, as lab and field monitoring data for the investigated embankment are not available. Finally, due to the incapability of a single constitutive hypothesis to simulate the mechanical behavior of an embankment dam under different loading conditions within its lifetime, several different constitutive models and sets of parameters had to be used. The artificial strategy of adopting different constitutive models for different loading conditions may be avoided with the use of novel visco-plastic constitutive relations for such granular materials.

2. Cokal CFRD

The Cokal Dam is an 83-m-high CFRD with a crest length of 605 m that is being built for irrigation and flood prevention in northwest Turkey at the Thracian peninsula. The dam site is located less than 10 km from an extension of the North Anatolian Fault under the Marmara Sea. Positioned in a wide canyon, the dam geometry permits the use of the plane-strain analogy utilized in this study. A typical cross-section of the dam is shown in Fig. 1a along with a selection of the materials that will be used at the site. The side slopes are 1H:1.4 V, whereas the face plate is 50 cm thick with a 0.3% reinforcement ratio.

The Cokal Dam was modeled and analyzed using the general purpose finite element software DIANA [14]. The high aspect ratio of the dam (crest length/height = 600 m/83 m = 7.2) allows for an idealization of the system as a 2-D plane-strain model. A total of 4600 six-node isoparametric plane-strain triangular elements with a three-point integration scheme were used in modeling the rockfill, whereas 54 three-node infinite shell elements, with each node having two in plane and one rotational degree of freedom, were used to represent the face plate. The infinite shell formulation, based on the isoparametric degenerated solid approach given in DIANA [14], introduces two shell hypotheses, i.e., the normals remain straight in the element and the stress perpendicular to the axis of the element is zero. Embedded reinforcements, which do not have degrees of freedom of their own, are smeared in the face

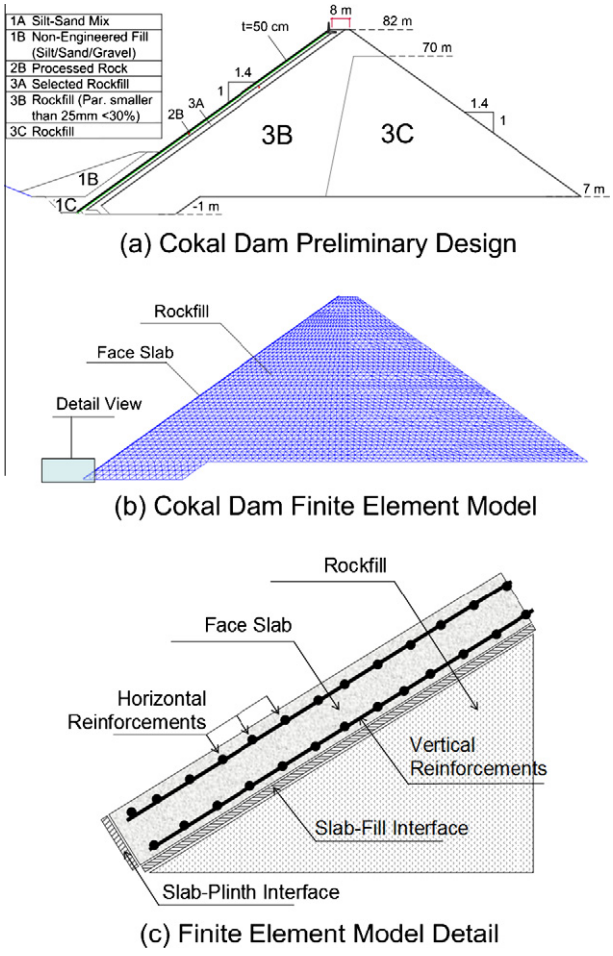

Fig. 1. The Cokal Dam and the finite element model.

slab elements. The strains of the embedded reinforcement elements are computed from the displacement field of the mother element, implying a perfect bond between the reinforcement and the material. The face plate elements were connected to the rockfill with line interface elements, based on quadratic interpolation, describing the relationship between the normal and shear tractions and the relative normal and shear displacements at multiple nodes. A nodal interface element was used at the bottom of the face plate to properly model any possible separation from the foundation at the plinth. The Cokal Dam rests on medium-hard rock with a Young's modulus that is approximately two orders of magnitude greater than that of the dam material; therefore, the foundation of the dam was not included in the model, and the base was assumed to be a fixed support. A sketch of the modeled constituents of the Cokal Dam is shown in Fig. 1c.

3. Material modeling

The various constitutive models used in the analyses of the Cokal Dam are described in this section (compressive stresses are expressed as negative values in this work, whereas tensile stresses are expressed as positive.)

3.1. Reinforced concrete

The constitutive model used for concrete is based on the total strain fixed-crack model [15]. The compressive behavior is defined by a parabolic response, with f_c defining the peak strength (Fig. 2).

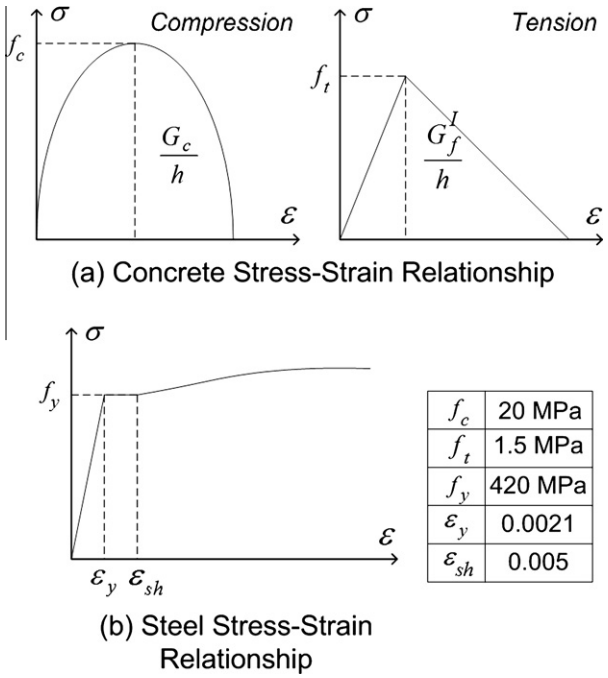

f_c	20 MPa
f_t	1.5 MPa
f_y	420 MPa
ε_y	0.0021
ε_{sh}	0.005

Fig. 2. Constitutive relations for a reinforced concrete face plate.

The crushing behavior and ultimate strain are governed by the compressive fracture energy G_c so that the model is objective and mesh-independent. The tensile behavior is modeled by using a linear softening function beyond the tensile strength f_t, with the ultimate tensile strain based on the tensile fracture energy G_f^I. The utilized tensile-compressive constitutive relationships are presented in Fig. 2a and b, respectively, with h denoting the effective element size. A typical strain hardening diagram was chosen for the embedded reinforcement with the stress–strain diagram as given in Fig. 2c, where f_y and ε_y represent the yield strength and strain, respectively.

3.1.1. Rockfill constitutive model: static loading

Triaxial experiments conducted on rockfill specimens reveal the following [16]: (a) the stress–strain behavior of rockfill material is nonlinear, inelastic and stress-dependent; (b) an increase in the confining pressure tends to increase the values of the peak deviatoric stress, axial strain and volumetric strain at failure; and (c) an increase in the size of the particles results in an increase in the volumetric strain at the same confining pressure. A modified Mohr–Coulomb formulation [17], as implemented in [14], was used in this study to model (1) the hardening of the rockfill with increasing shear stress, (2) the volumetric deformations and (3) the dependency of the mechanical properties on the confinement stress. This constitutive relationship utilizes nonlinear elasticity combined with a smooth, hardening shear yield surface and a circular-shaped compression cap. Within the failure surfaces, nonlinear elasticity is employed through the use of a power law. The compression modulus K_t is assumed as some power $(1-m)$ of the current mean effective stress level $p' = 1/3(\sigma'_{xx} + \sigma'_{yy} + \sigma'_{zz})$ and the reference compression modulus K_{ref} as given in (1):

$$K_t = K_{ref}\left(\frac{p' + p'_t}{p_a}\right)^{1-m} \tag{1}$$

where p_a and p'_t represent the atmospheric pressure and a compression offset value used to improve the model performance for tension, respectively. The yield function for this model is a double hardening model in which the shear and compressive failures are

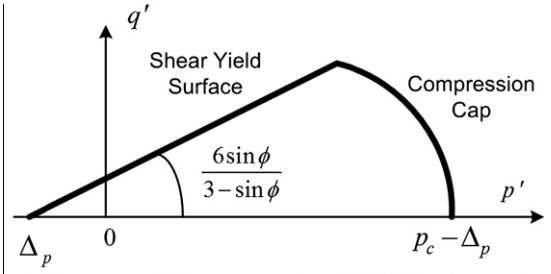

(a) Shear and Compression Yield Surfaces in p'-q' Space

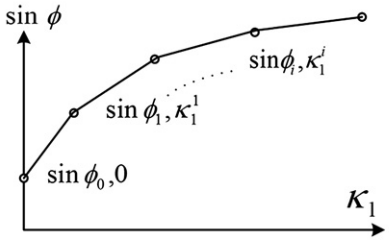

(b) Multi-Linear Hardening of Friction Angle w.r.t. Internal Variable κ_1

Fig. 3. Rockfill constitutive model.

uncoupled. In $p'-q'$ space, where q' denotes the deviatoric stress, the functions (f_1) and (f_2) defining the shear and compression failure surfaces (Fig. 3a) can be written as:

$$f_1 = \frac{q'}{R_1(\theta)} - \frac{6\sin\phi}{3-\sin\phi}(p'+\Delta p') = 0 \tag{2}$$

$$f_2 = (p'+\Delta p')^2 + \frac{2}{9}q'^2 - p_c^2 = 0 \tag{3}$$

where ϕ is the friction angle, $\Delta p'$ is the pressure shift for the shear yield surface, p_c is the preconsolidation pressure, and $R_1(\theta)$ is a function of Lode's angle θ. The direction of the inelastic strain rate is set by the plastic potential surfaces g_1 and g_2 given in Eqs. (4) and (5), where ϑ represents the angle of dilatancy.

$$g_1 = q' - \frac{6\sin\vartheta}{3-\sin\vartheta}(p'+\Delta p') \tag{4}$$

$$g_2 = (p'+\Delta p')^2 + \frac{2}{9}q'^2 - p_c^2 \tag{5}$$

The evolution of the shear yield surface is governed by a multi-linear variation of the sine of the friction angle ($\sin\phi = \sin\phi(\kappa_1)$) with respect to an internal model variable κ_1 (Fig. 3b), while the evolution of the compression cap is governed by changes in the preconsolidation pressure p_c with respect to an internal variable κ_2. A detailed description of this model is provided in Appendix A.

Because well-documented test results were not available for the filler material of the Cokal Dam, test results on the rockfill material from [16] were used to calibrate the material model in this study. The constitutive model was calibrated to triaxial tests that were conducted at three levels of confining stress (i.e., 0.35, 0.7 and 1.1 MPa) using the deviatoric stress-axial strain and volumetric strain-axial strain results. Hardening of the shear yield surface is prescribed by the multi-linear variation of the sine of the friction angle in this model. Calibration of the hardening of the compression cap was not attempted, as the stress levels were below the stress state at which the cap yield surface is reached. The final parameters for the constitutive model are presented in Table 1. A

Table 1
Parameters for the rockfill plasticity model.

Parameter	Value
p_t'	0.2 MPa
$\Delta p'$	0.02 MPa
p_c	3.5 MPa
K_{ref}	13.3 MPa
m	0.22
$\sin\phi(\kappa_1^i)$[a]	0.52(0.00)/0.66(0.007)/0.70(0.014)/0.74(0.036)/0.90(0.44)
$\sin\phi_{cv}$	0.755
υ	0.32

[a] Refer to Fig. 3b.

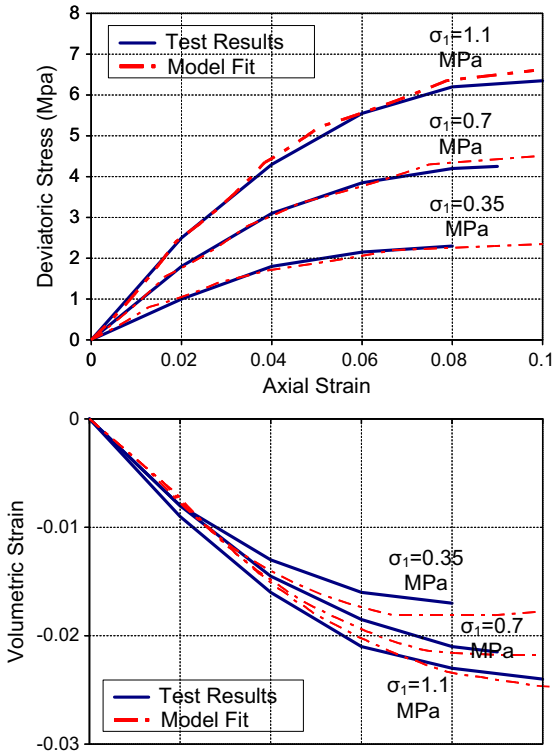

Fig. 4. Comparison of triaxial test results [16] vs. model predictions.

comparison of the model estimations and the triaxial test results is provided in Fig. 4.

3.1.2. Rockfill constitutive model: time-dependent deformation

The long-term behavior of the rockfill material is simulated using a visco-elastic constitutive relationship [14,18] with a creep function $J(t,s)$ defining the time-dependent equivalent stiffness $\tilde{E}(t)^j$ given in (6) for each (j^{th}) plane-strain element.

$$\tilde{E}(t)^j = \left\{\frac{1}{\Delta t}\int_t^{t+\Delta t} J(t+\Delta t,s)ds\right\}^{-1} \tag{6}$$

The creep function $J(t,s)$ is defined by a Dirichlet series that can be interpreted as a Kelvin chain with two elements, a spring complemented by a spring-damper system, as presented in Fig. 5. The modulus E_0^j represents the stiffness of the j^{th} plane-strain element at the end of the impounding stage and was obtained from Eq. (1) for a constant Poisson ratio (υ). The viscosity of the added damper $\eta_1^j = \lambda_1 E_1^j$ is expressed in terms of the retardation time λ_1 and the modulus of the added spring E_1^j. E_1^j was expressed as a constant multiple of E_0^j for all plane-strain elements. These model parameters were calibrated by comparing the simulated long-term deformation of the dam crest

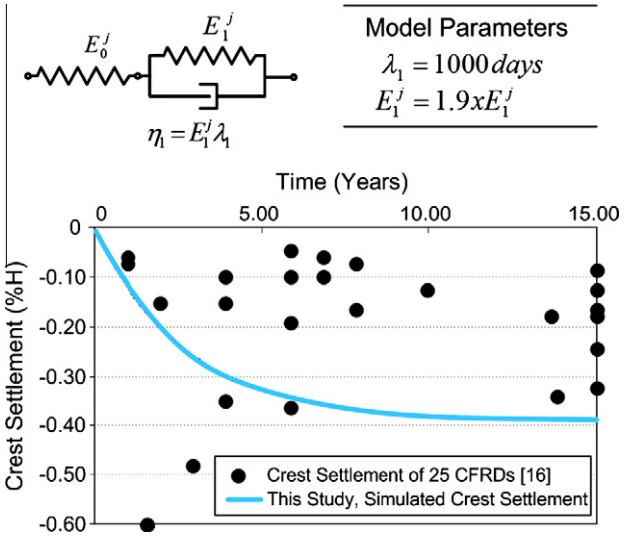

Fig. 5. Time-dependent sett of the Cokal Dam crest in comparison with CFRD field observations [19].

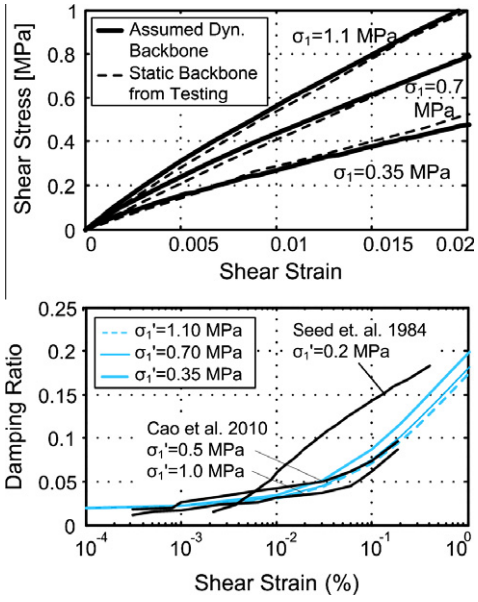

Fig. 6. Performance of the dynamic model.

and the data obtained from field monitoring of many CFRDs [19]. As presented in Fig. 5b, the permanent deformation at the crest of the Cokal Dam was 0.4% of the dam height (H), which compares reasonably well with the observed behavior of many dams. Further details of this creep model, generally used in long-term creep simulations, are provided in Appendix A.

3.1.3. Rockfill constitutive model: dynamic loading

A modified Ramberg–Osgood formulation [14] described by Eqs. (7) and (8) was used to simulate the stiffness degradation and hysteretic damping of the rockfill material under cyclic shear strain. The parameters α and β that define the dynamic backbone function for this formulation are determined using the reference shear strain (γ_r) and the maximum damping value (ξ_{max}).

$$\gamma_{xy} = \frac{\sigma_{xy}}{G}(1 + \alpha|\tau_{xy}|^{\beta}) \tag{7}$$

$$\alpha = \left(\frac{2}{\gamma_r G}\right)^{\beta} \quad \& \quad \beta = \frac{2\pi\xi_{max}}{2 - \pi\xi_{max}} \tag{8}$$

$G = G_{ref}(p'/p_a)^{0.5}$ is the tangent shear modulus in the above formulation, defined by the current mean effective stress p', the atmospheric pressure p_a and the reference shear modulus G_{ref} = 30 MPa. The unloading and reloading behavior is described by Masing's rules [20].

The dependency of the damping ratio and stiffness degradation on the confining stress [21–23] was considered by defining the reference shear strain in Eq. (7) as a function of the mean stress p' ($\gamma_r = a\exp(bp')$). The parameters a = 0.0042 and b = 0.62 were obtained by calibrating the backbone curves at three confinement levels to tests results in [16], as given in Fig. 6. The shear strain vs. damping ratio curves obtained with the model compare well with the test results for Changheba Dam [23] rockfill, but are somewhat lower than the curves suggested for Oroville Dam material in [21]. To account for the low damping provided by the Ramberg–Osgood formulation at very small shear strains, a 2% viscous damping was added to the model using Rayleigh damping. Separate values of γ_r for each plane-strain element within the embankment were calculated based on the mean effective stress p' of an element at the end of impoundment (EoI) stage.

3.2. Interface modeling

Experimental data on the interface behavior of CFRD systems are rather limited [12,24]. Monotonic and cyclic shear tests on the interface were conducted in [24], leading to the conclusion that failure of the interface is a combination of contact and filler failure. Residual friction coefficients between 0.6 and 0.8 were obtained. A friction-dominated response with observed volumetric dilation behavior was presented in tests conducted for the interface between a concrete slab and a gravel cushion layer in [12]. Consistent with the findings of these studies, the interface between the slab and the cushion layer was assumed to be governed by frictional behavior simulated using a simple Mohr–Coulomb plasticity model [14,25]. The Coulomb friction model employs the following yield (f_I) and plastic potential (g_I) surfaces defined in terms of the normal traction t_n and the tangential traction t_t.

$$f_I = \sqrt{t_t^2} + t_n\tan\phi_I - c_I = 0 \tag{9}$$

$$g_I = \sqrt{t_t^2} + t_n\tan\vartheta_I \tag{10}$$

where $\tan\phi_I$ and c_I are the friction coefficient and the cohesion, respectively. *Tan* ϑ_I represents the tangent of the angle of dilatancy. The rate of plastic displacement $\Delta\dot{u}^p$ is governed by:

$$\Delta\dot{u}^p = \dot{\lambda}\frac{\partial g}{\partial t} \tag{11}$$

where $\dot{\lambda}$ is a multiplier. The tangent stiffness matrix is nonsymmetrical if the friction angle is not equal to the dilatancy angle ($\phi_I \neq \vartheta_I$). The interface element was calibrated to the test results given in [12] for a concrete-gravel layer contact, as shown in Fig. 7. Except for the later stages of sliding, in which dilation is overestimated, the agreement is quite reasonable.

4. Phased analysis of the Cokal Dam

CFRD deformations start at the construction stage only to stabilize in the very long term. The behavior is dependent on the intact particle strength, rockfill gradation, minerology and foundation conditions as well as construction technique. Early CFRD structures

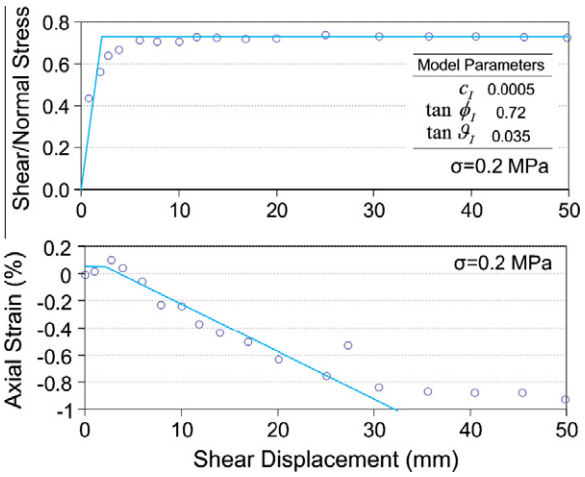

Fig. 7. Comparison of shear friction tests [12] vs. model predictions.

built without proper compaction settled up to 5.5–6% of their height (H) in their lifetime; the use of vibro-cylinders and a better preparation of the rock material led to reduced settlement values (<0.5% H) in the long term [26]. During the impounding stage, the CFRD deformations are small. Observations of crest settlement ranging between 0.02–0.05 and 0.1–0.15% H after the initial reservoir filling were reported in [27] for rockfill embankments with very high strength and intermediate minerology, respectively. Some exceptions to these settlement limits were observed, attributed to the low modulus of elasticity and relatively large height of these systems [19].

The most important aspect of performance for a CFRD dam is usually seen as the flexibility of the face plate to conform to rockfill displacements without extensive cracking. During construction, the settlement of rockfill causes compressive stress on approximately 90% of the face plate [28]. Hence, settlement of the embankment under the face plate is a loading condition for the plate. Modeling of the construction, loading stages and long-term settlements is thus important in realistically predicting the behavior of the face plate. In order to properly investigate these stages in the lifetime of a CFRD, a phased analysis technique was used in this study. The rockfill was placed in 27 stages using 3-m lifts. The concrete plate was created on the top of the rockfill afterwards, connected to the rockfill slope with interface elements (corresponding to the end of construction (EoC) stage). The impounding process was then modeled with the reservoir rising to the maximum water level (MWL) in 27 steps (EoI). Creep of the rockfill was taken into consideration after the EoI stage, and the visco-elastic model was used for the rockfill (deactivating plasticity) to determine the accumulating displacements in the embankment and their effects on the face plate in the long term. Since a limited zone of the embankment reached yielding in the plasticity model at the EoI stage, such an approach was appropriate. The sequence of modeling, from the construction stage to the end of long-term analysis, is presented in Fig. 8.

4.1. Behavior of the Cokal Dam during construction, impoundment and long-term deformation

The state of vertical stress at the EoC and EoI stages for the Cokal Dam is presented in Fig. 9a. Impounding changes the state of stress relatively significantly only near the upstream face of the dam. The maximum compressive vertical stress is around −1.4 MPa at the core of the dam near the base. A maximum settlement of around 30 cm is observed at the center of the rockfill. The long-term deformation of the fill at the end of 14 years is compared to the EoI deformations in Fig. 9c.

In order to properly display the force transfer mechanism between the plate and the rockfill, the face plate was modeled initially as linear elastic. The variation of the plate axial stresses during impounding is presented in Fig. 10a as a function of distance from the plinth along the dam face for the EoI stage. Before impounding, the plate is under uniaxial compression due to its own weight, with a maximum value of approximately −0.9 MPa at the bottom. Due to rising of the reservoir, the face plate begins to experience tensile stresses (Fig. 10a), leading to separation from the plinth for a reservoir level of approximately 27 m. At the MWL, the tensile stresses on the plate are as high as 4 MPa near the bottom. By comparing the tensile stress demand with the tensile strength (1.5 MPa), one can easily justify the need for nonlinear modeling of the face plate.

In the long term, tensile stresses on the face plate are incrementally reduced while the creep deformations increase (Fig. 10b). Settlement of the rockfill causes compressive stresses on the plate pulling it towards the foundation, confirming the observations in [28]. For a long-term crest settlement of 0.10% of the dam height, the maximum tensile stress is reduced to 3 MPa. On almost 80% of the face plate, compressive stresses are again observed for a settlement of 0.3% H; the tensile stress near the foundation is reduced to 1 MPa, whereas compressive stresses as high as −1.5 MPa are observed near the crest.

The level of axial stress on the face plate is limited by the ability of the cushion layer–face plate interface to transfer shear force. In order to investigate the nature of this stress transfer, the shear/normal stress ratio along the interface between the face plate and the rockfill was studied (Fig. 11). In Fig. 11, a positive shear/normal stress ratio implies that the stress on the face plate is directed towards the crest of the dam; i.e., the rockfill is supporting the face plate. On the other hand, a negative shear stress ratio implies that the rockfill is pulling the face plate towards the plinth. The initial state of stress given in Fig. 11a shows that the rockfill is supporting the face plate at the EoC. A reservoir level rise to H = 42 m significantly decreases the shear stress ratio, but the rockfill still supports the plate. For the MWL, shear stress is reversed only along the bottom 10 m of the face plate, which accounts for the reduction in the tension on the plate from the maximum value shown in Fig. 10a near the plinth. The friction capacity of the interface is not overcome during impounding except near the bottom, at the plinth. Long-term settlement changes the pattern at the EoI stage considerably near the crest of the dam. The shear stress ratio on the face

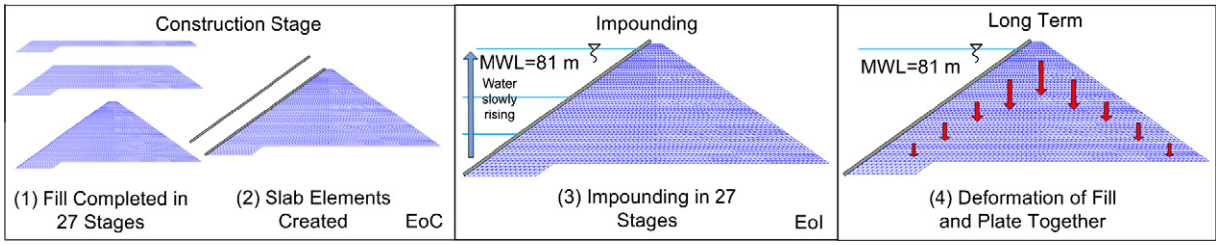

Fig. 8. Analysis schemes to simulate short- and long-term behavior.

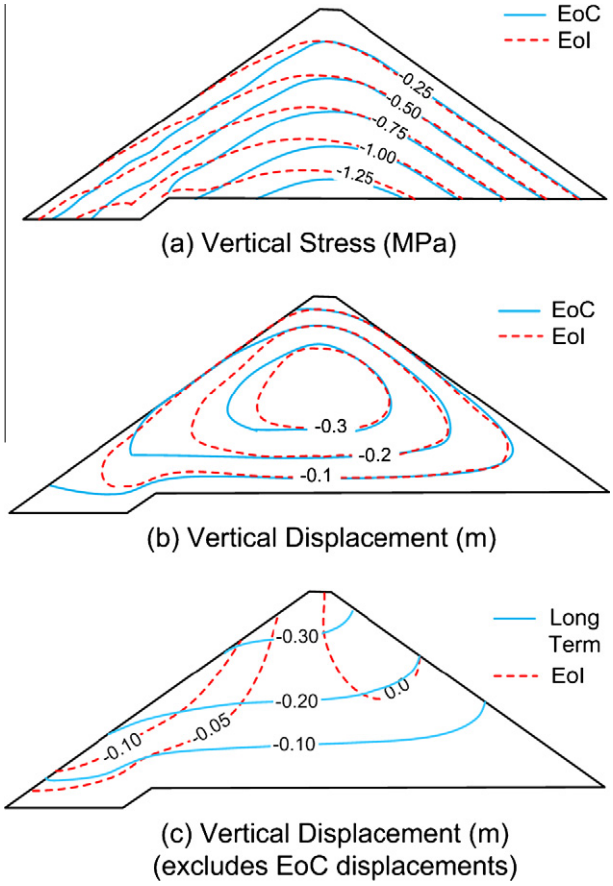

Fig. 9. Vertical stresses and displacements of rockfill.

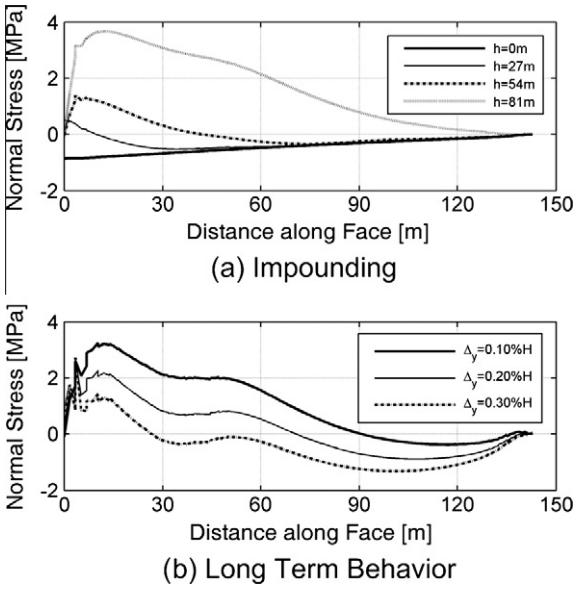

Fig. 10. Axial stress on the face plate in the short and long term.

plate for the bottom half changes very little, as shown in Fig. 11b, but near the crest, the direction of the shear stress is observed to reverse. This reversal leads to a reduction in the tension on the face plate, i.e., the rockfill pulls the face plate down during settlement. The top half of the face plate regains its compression status as a result of this settlement (for crest settlement, $\Delta_y > 0.10\%H$).

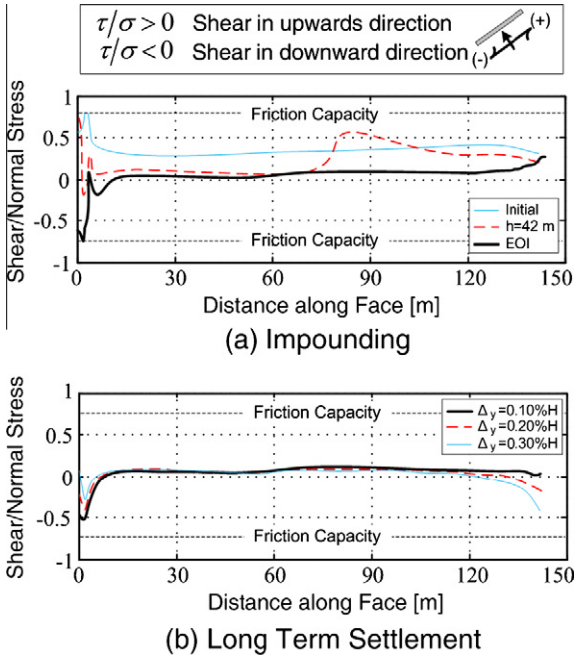

Fig. 11. Variation of shear/normal stress ratio during impounding and settlement of the fill.

4.2. Face plate nonlinearity and cracking

As shown above, the tensile stresses on the face plate of the Cokal Dam are strong enough to lead to cracking. Incorporating the total strain crack model for the reinforced concrete face plate with embedded reinforcement, the stresses on the face plate were recalculated for the impounding stage and the long term, as given in Fig. 12a and b, respectively. The axial compressive stress on the plate incrementally increases from an initial value of −0.9 MPa to give way to tensile stresses during impounding, similar to the results provided for the analysis with linear elastic face plate behavior (Fig. 10). The first sign of nonlinearity is the separation from the plinth, occurring when the reservoir level reaches 30 m (Fig. 12a). Cracking takes place in the plate after this stage, leading to a redistribution of the stresses to the reinforcement. The tension (cracking) zone spreads higher on the plate as the reservoir level rises. The plot of the stresses on the face plate for the MWL shows the presence of cracks in the first 45 m of the plate near the plinth base. In the long term, settlement of the fill reduces the tensile stresses on the face plate, leading to compression (Fig. 12b). For a crest settlement of 0.3% of the dam height, 4/5 of the plate reverts back to axial compression, similar to the results given in Fig. 10. In the remaining portion of the plate, the tensile stresses are reduced; however, the cracked region near the plinth does not regain its integrity (Fig. 12b).

The crack widths on the face plate near the plinth were estimated using the empirically well-established Gergely–Lutz expression [29], which is commonly used in reinforced concrete design [30], relating the maximum crack width w_{max} to three variables: the reinforcement steel strain at the crack (ε_{scr}), the concrete cover over the reinforcement d_c and the area of concrete around each bar A:

$$w_{max} = 2.2\beta_{GL}\varepsilon_{scr}\sqrt[3]{d_c A} \tag{12}$$

where β_{GL} is a factor that accounts for the strain gradient within the member. Reinforcement stresses at the bottom of the face plate increase during impounding and barely reach the yield stress at the

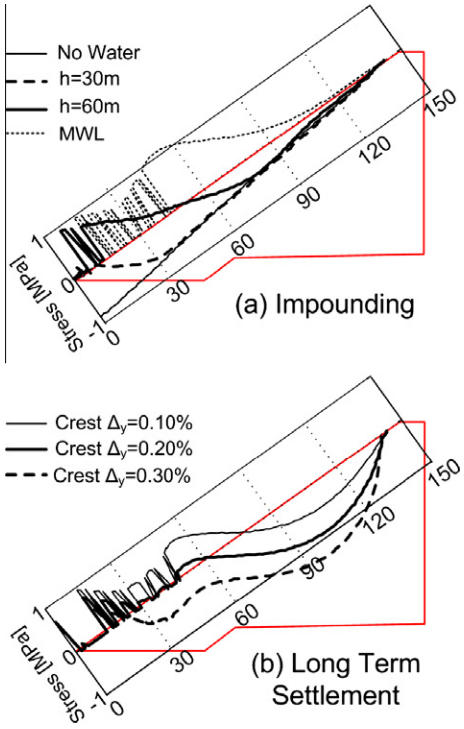

Fig. 12. Variation of face plate stresses during impounding and settlement of the fill.

MWL (Fig. 13a). Crack widths as large as 1.0 mm are obtained for this case, while the average crack width is around 0.5 mm for a 45-m section of the face plate (Fig. 13a). Long-term settlement of the rockfill does not significantly decrease the maximum reinforcement stress, but it reduces the average stress in the bottom 1/3 of the face plate, as shown in Fig. 13b. A reduction in the maximum crack width to 0.7 mm is observed, with a significant reduction in the cracked region (down to <30 m) and in the average crack width (down to 0.4 mm) of the face plate (Fig. 13b). As shown in Fig. 12b, the existing cracks do not close at the bottom of the plate, but their extent and width are reduced. Perhaps this phenomenon explains why the seepage from impounded dams is quite high right after impounding, decreasing and approaching a steady state in the lifetime of the structure as in the Foz de Areia Dam [31]. The initial seepage level of 236 L/s reduced to a steady state level of 70 L/s 5 years after filling the reservoir for this system.

The shear/normal stress ratio for the face plate is presented in Fig. 14 for impounding and long-term settlement of the fill. The use of nonlinear properties for the face plate did not result in significant changes from the earlier results obtained with the linear-elastic plate assumption (Fig. 11). For both cases, the shear/normal stress ratio on the interface was far smaller than the transfer capacity of the layer between the plate and the rockfill.

5. Effect of earthquake loading on the Cokal Dam

A site-specific seismic hazard study was conducted for the Cokal Dam, establishing a design response spectrum for operational-based earthquake (OBE) and maximum design earthquake (MDE) levels [32]. OBE events are defined as earthquakes with a return period of 144 years in accordance with the national practice; during an OBE event, the dam must sustain minimum damage and must remain operational. For nonlinear transient time history analyses of the Cokal Dam, three different time histories that were matched to the OBE target spectra were used. The ground motions

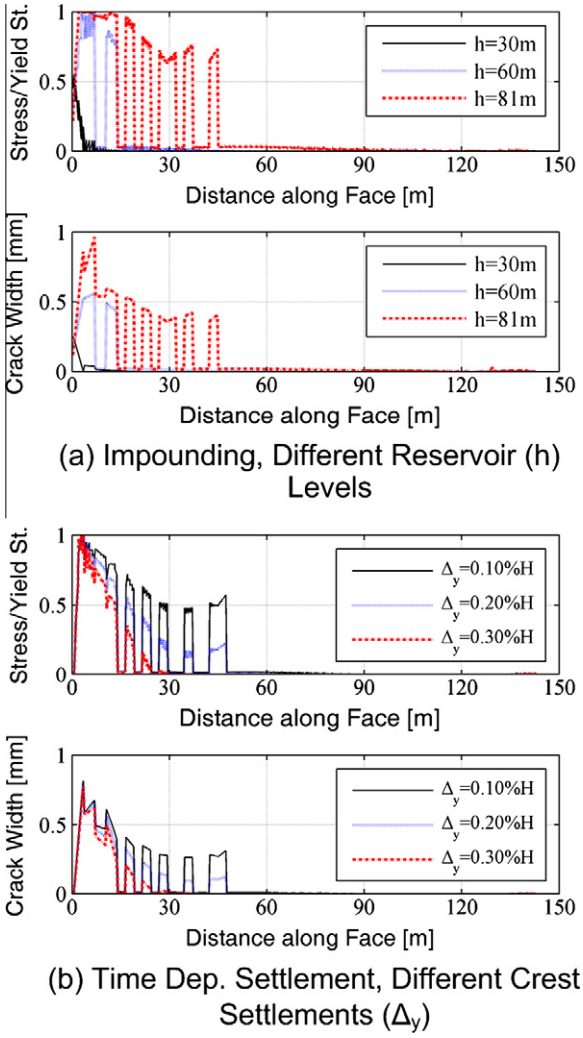

Fig. 13. Face plate stress and crack width during impounding and settlement of the fill.

OBE1, OBE2 and OBE3, with PGA levels of 0.28, 0.22 and 0.25 g, respectively, are presented in (Fig. 15) along with a comparison of the spectrum of these motions and the target spectra for the Cokal Dam site. After the EoI stage, the plasticity model for the rockfill was deactivated, and transient analyses of the Cokal Dam were conducted using the modified Ramberg–Osgood formulation for the rockfill. For these analyses, the initial shear modulus $G = G_{ref}(p'/p_a)^{0.5}$ for each element of the finite element model was obtained in accordance with the effective stress p' on the element at the end of the static analysis (EoI stage). The initial shear modulus along the centerline of the dam (normalized with respect to the modulus G_b at the base) increases with depth (z) from the crest as given in Fig. 16, comparing well with the field data obtained from 12 actual earth dams [33]. Newmark's method with $\gamma_n = 1/2$ and $\beta_n = 1/4$ was chosen as the time stepping algorithm for the transient analyses and uniform base excitation was applied to the model with equivalent inertial forces in the customary fashion. A 2% viscous damping was added to the model using Rayleigh damping to account for the deficiency of the Ramberg–Osgood model in providing damping at small shear strains.

Horizontal and vertical displacement time histories obtained at the crest of the dam are presented in Fig. 17a and b, respectively. A maximum lateral deformation of approximately 40 cm was observed for OBE3. The permanent lateral deformations for all events are less than 5 cm. The maximum vertical deformation is around

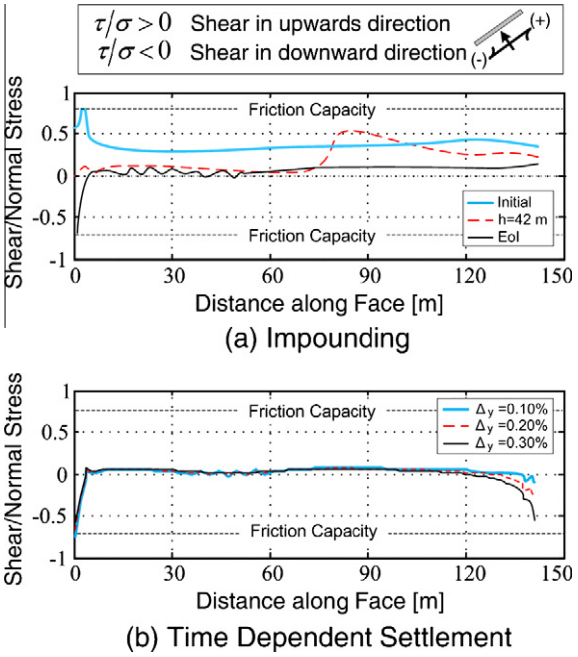

Fig. 14. Variation of shear/normal stress ratio during impounding and settlement of the fill.

10 cm, with a negligible residual settlement. The time history of plinth opening-closing, presented for the three events in Fig. 17c, shows that the gap between the plinth base and the face plate (at approximately 1.0 cm before the earthquake) tends to close after the ground motion.

Time histories for shear strains at various elevations along the dam centerline (Fig. 18) are presented in Fig. 19a for the OBE1 event. At elevations of 18 and 38 m along the centerline of the dam, the maximum shear strain is around 0.3%; the residual strains are around 0.1%. Near the crest of the dam, the maximum shear strain is much lower (around 0.15%). The envelope of maximum shear strains in the embankment computed over the whole time history of OBE1 is presented in Fig. 19b. The shear strain envelopes for the OBE2 and OBE3 ground motions are similar to this distribution as well.

The change in the nature of the earthquake motion as it travels through the embankment was investigated by evaluating the

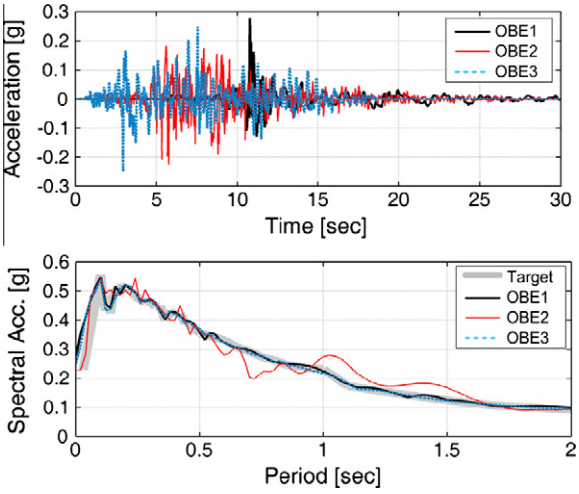

Fig. 15. Earthquake ground motion time histories.

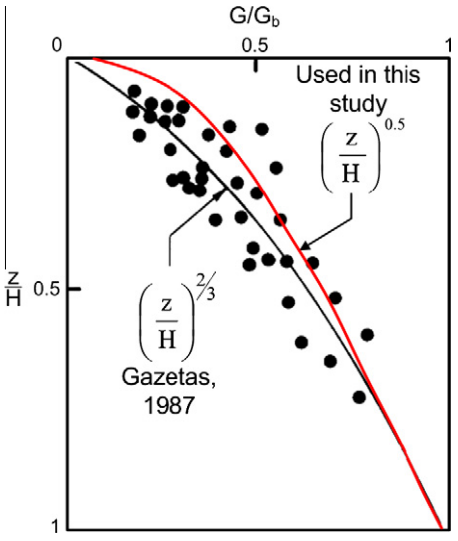

Fig. 16. The variation of stiffness along the centerline of the dam (original figure used from [33]).

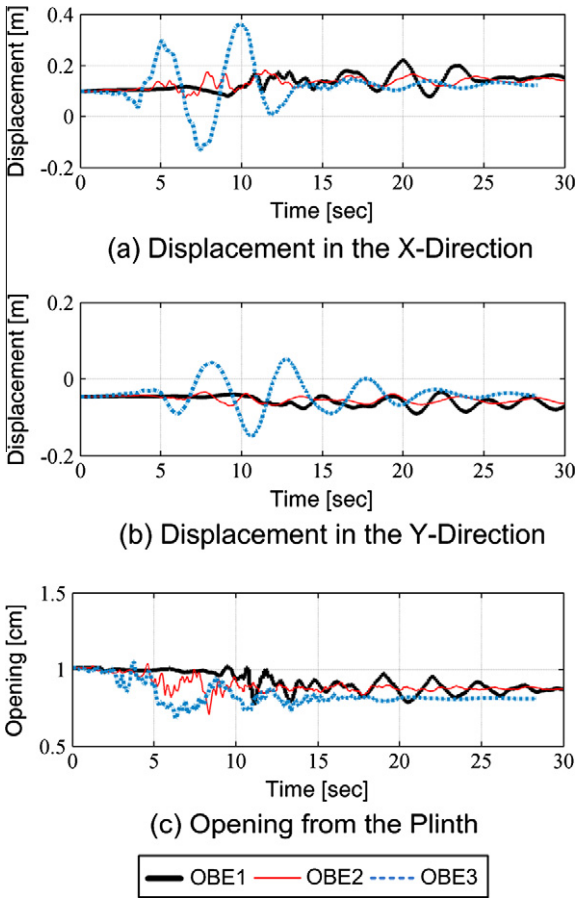

Fig. 17. Time history response during an OBE event.

transfer function between the base excitation and the acceleration at different elevations along the centerline of the embankment (SM1, SM2, SM3, Fig. 18). As shown in Fig. 20, the ground motion is amplified nearly two times at various frequencies up to 5 Hz at the crest. Notably, for the first peak frequency, the motion is amplified more at the middle (SM2, Fig. 18) and bottom of the

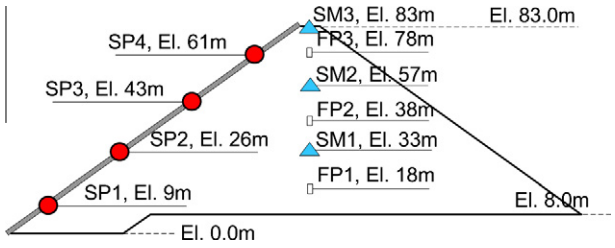

Fig. 18. Selected observation locations at the face plate and embankment for the Cokal Dam.

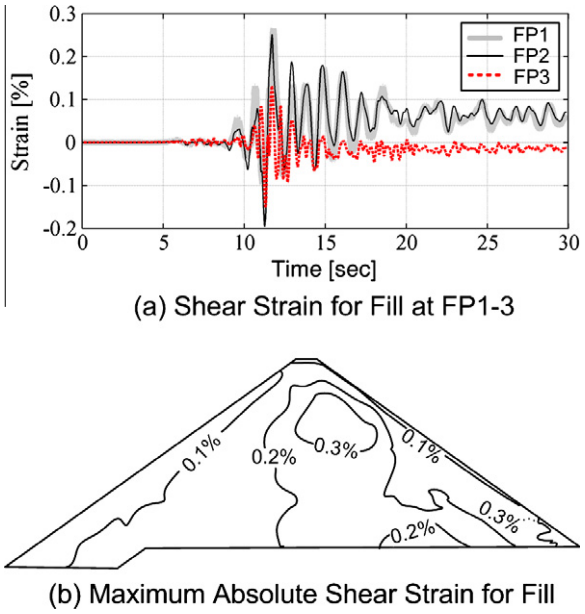

Fig. 19. Shear strain time histories and maximum shear strains for the OBE1 event.

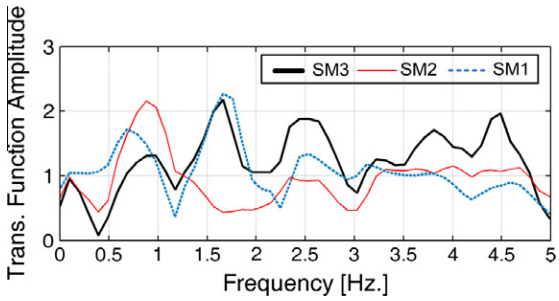

Fig. 20. Transfer function amp. at different heights along the dam centerline for OBE1 event.

embankment (SM1, Fig. 18) as compared to the crest. For the second peak, deamplification of the ground motion at the middle of the embankment is observed. Such an amplification within the embankment may explain the distribution of the shear strains provided in Fig. 19. The first peak caused the large shear strains observed below the crest while the second peak might be responsible for the higher strains occurring very close to the foundation.

Variations in the axial stresses of the face plate, for four different elevations (SP1, SP2, SP3, SP4, Fig. 18), are presented in Fig. 21 for the OBE1 event. At SP1 and SP2, which are lower on the face plate, the plate is under tension (due to impounding) before the earthquake loading. After approximately 10 s, the tensile demand

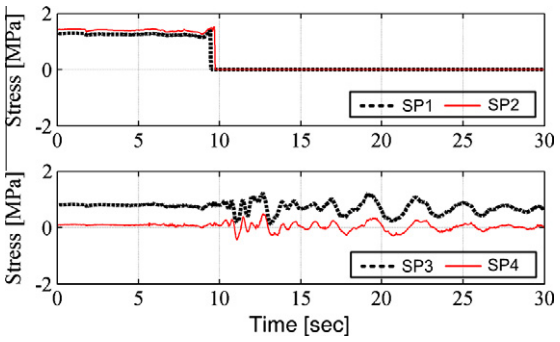

Fig. 21. Variation of axial stress within the face plate for the OBE3 event.

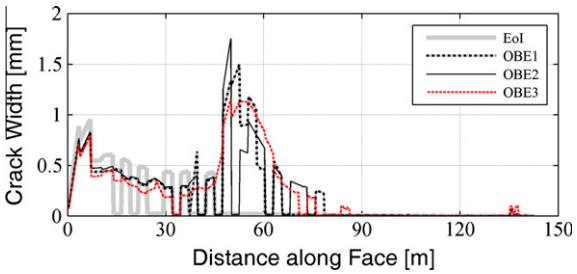

Fig. 22. Estimated crack width after earthquake loading.

on the face plate increases, reaching the tensile capacity. The stresses are reduced to zero for the rest of the motion, and the reinforcements account for the integrity of the plate. The tensile stresses do not reach the tensile strength of the face plate at locations SP3 and SP4. While location SP3 is always under tension during the period of ground motion, at SP4, the stress on the face plate oscillates between compression and tension.

The final state of the cracking on the face plate at the end of the earthquake motions is presented in Fig. 22. After the earthquake motion, the cracking on the face plate extends by approximately 35 m towards the crest of the dam. The crack width at the bottom of the plate decreases, while new cracks with widths as large as 1.7 mm develop in the face plate. For the OBE3 event, some small cracking at the crest of the dam is observed, possibly due to the separation of the plate from the crest of the dam.

6. Summary and conclusions

In this study, the performance of the face plate of a CFRD was investigated, with a focus on crack development during impounding of the dam and long-term deformation of the rockfill. The following conclusions can be drawn based on the analysis results.

- The friction capacity of the face plate–cushion layer interface was not exceeded during impounding or long-term deformation of the dam.
- Impounding of the reservoir caused tensile cracking at the bottom 1/3 of the face plate. The majority of the face plate was under a low level of tensile stress for the maximum reservoir level. The maximum crack width (1.0 mm) on the face plate after impounding was near the plinth base. The average crack width on the bottom 1/3 of the face plate was around 0.5 mm.
- Long-term settlement of the rockfill significantly changes the state of stress on the face plate; the rockfill settlement compresses the plate. As much as 60% of the face plate reverted back to the compressive state for a long-term settlement quantified by 0.20% H at the dam crest. In the long term, the extent of

the cracked region was significantly reduced as well. The average crack width within this region was reduced from 0.5 mm to 0.4 mm, with the maximum crack width decreasing from 1.0 mm to 0.7 mm.
- The predicted crack widths for the plate were above the serviceability limits for concrete structures (<0.1 mm) in hazardous conditions [30]. If these cracks are not filled during operation by sediment flow, corrosion and sudden increases in cracking and seepage in the face plate can be expected.
- For OBE-level earthquakes, significant spreading of the cracking on the face plate was observed. The maximum crack width also changed significantly after the event, implying that the reinforcement ratio for the case study may not be adequate.

Acknowledgements

This study has been conducted with the funding provided by The Scientific and Technological Research Council of Turkey (TUBITAK) under the Grant MAG108M491. I would like to express my gratitude for the comments on the original manuscript provided by Dr. Baris Binici. I would also like to thank the anonymous reviewers for their valuable comments and suggestions.

Appendix A. Rockfill plasticity

The nonlinear elasticity, yield surfaces, flow and hardening rules utilized in the plasticity model for the rockfill are presented below [14,17].

A.1. Nonlinear elasticity

Elastic behavior is assumed to be isotropic in this model. The tangential compression modulus sets the rate relationship between the current mean effective stress p' and the elastic volumetric strain ε_v^e as given in Eq. (A.1). Using the tangent modulus as a function of the mean stress p', the reference compression modulus K_{ref} and the power parameter m, the volumetric stress–strain relationship given in Eq. (A.3) is obtained.

$$\dot{p}' = -K_t \dot{\varepsilon}_v^e \tag{A.1}$$

$$K_t = K_{ref}\left(\frac{p' + p_t'}{p_a}\right)^{1-m} \tag{A.2}$$

$$\left(\frac{p' + p_t'}{p_{ref}'}\right)^{m-1} dp' = K_{ref} d\varepsilon_v^e \tag{A.3}$$

where p_a and p_t' represent the atmospheric pressure and a compression offset value used to improve the model performance for tension, respectively. Assuming isotrophy and a constant Poisson ratio (υ), one can define a tangent shear modulus G_t (A.4).

$$G_t = \frac{3}{2} K_t \frac{1-2\upsilon}{1+\upsilon} \tag{A.4}$$

A.2. Yield criteria

Plastic behavior is controlled by shear (f_1) and compressive (f_2) yield surfaces that are assumed to be uncoupled.

$$f_1 = \frac{q'}{R_1(\theta)} - \frac{6\sin\phi}{3-\sin\phi}(p' + \Delta p') = 0 \tag{A.5}$$

$$f_2 = (p' + \Delta p')^2 + \frac{2}{9} q'^2 - p_c^2 = 0 \tag{A.6}$$

where q', ϕ and p_c are the effective deviatoric stress, the friction angle and the preconsolidation pressure, respectively. $\Delta p'$ is a pressure shift introduced to move the shear yield surface, simulating cohesive behavior. The function $R_1(\theta)$, given in Eq. (A.7), accounts for the difference in triaxial strength for compression and tension by making use of Lode's angle θ and the factor β_1.

$$R_1(\theta) = \left(\frac{1 - \beta_1 \sin 3\theta}{1 - \beta_1}\right)^{-0.229} \tag{A.7}$$

$$\beta_1 = \left(\frac{3+\sin\phi}{3-\sin\phi}\right)^{\frac{-1}{-0.229}} - 1/\left(\frac{3+\sin\phi}{3-\sin\phi}\right)^{\frac{-1}{-0.229}} + 1 \tag{A.8}$$

A.3. Flow rule

The direction of the inelastic strain rate is determined by the potential surfaces g_1 and g_2, implying an associative behavior in $p' - q'$ space and a non-associated flow in the deviatoric space.

$$g_1 = q' - \frac{6\sin\vartheta}{3-\sin\vartheta}(p' + \Delta p') \tag{A.9}$$

$$g_2 = (p' + \Delta p')^2 + \frac{2}{9} q'^2 - p_c^2 \tag{A.10}$$

The dilatancy angle ϑ is a function of the friction angle according to Rowe's stress dilatancy theory.

$$\sin\vartheta = \frac{\sin\phi - \sin\phi_{cv}}{1 - \sin\phi\sin\phi_{cv}} \tag{A.11}$$

where ϕ_{cv} is a constant value that can be conceived as the friction angle at constant volume.

A.4. Hardening behavior

The evolutions of the failure surfaces are uncoupled in this model. The hardening behavior for the shear failure surface is modeled through the evolution of the friction angle $\sin\phi = \sin\phi(\kappa_1)$. A multi-linear variation of the friction angle with respect to the internal variable κ_1 is specified. Both hardening and softening can be simulated with the prescribed multi-linear variation in this formulation (softening terms were not needed/utilized in this study). Changes in κ_1 for the model are tracked using the equivalent plastic deviatoric strain increment $\Delta\boldsymbol{\gamma}^p$ and a diagonal factor matrix $\mathbf{R}$ (Eq. (A.12)). The hardening behavior of the compression cap is modeled through evolution of the preconsolidation pressure, p_c, as a function of the internal variable κ_2. The variation in κ_2 is equal to the change in the volumetric plastic strain $\Delta\varepsilon_v^p$, as given in Eq. (A.13) (hardening of the compression cap was not utilized in this study.)

$$\Delta\kappa_1 = \sqrt{\left(\frac{2}{3}\right)(\Delta\boldsymbol{\gamma}^p)^T \mathbf{R} (\Delta\boldsymbol{\gamma}^p)} \tag{A.12}$$

$$\Delta\kappa_2 = -\Delta\varepsilon_v^p \tag{A.13}$$

A.5. Rockfill creep: visco-elastic model

The viscoelastic behavior of a material can be modeled using a creep function $J(t,s)$ which is used to obtain the time dependent mechanical properties. In a general form, the strain $\varepsilon(t)$ at any time t can be written as a function of a six by six dimensionless matrix $\overline{\mathbf{C}}$ and the stress rate tensor $\dot{\boldsymbol{\sigma}}$.

$$\boldsymbol{\varepsilon}(t) = \int_0^t J(t,s)\overline{C}\dot{\boldsymbol{\sigma}}(s)ds \tag{A.14}$$

$$\overline{\mathbf{C}} = \begin{bmatrix} 1 & -\upsilon & -\upsilon & 0 & 0 & 0 \\ -\upsilon & 1 & -\upsilon & 0 & 0 & 0 \\ -\upsilon & -\upsilon & 1 & 0 & 0 & 0 \\ 0 & 0 & 0 & 2(1+\upsilon) & 0 & 0 \\ 0 & 0 & 0 & 0 & 2(1+\upsilon) & 0 \\ 0 & 0 & 0 & 0 & 0 & 2(1+\upsilon) \end{bmatrix} \tag{A.15}$$

The strain increment $\Delta\boldsymbol{\varepsilon} = \boldsymbol{\varepsilon}(t_{i+1}) - \boldsymbol{\varepsilon}(t_{i+1})$ can be expressed as below:

$$\Delta\boldsymbol{\varepsilon} = \int_0^{t_i} [J(t_{i+1}, s) - J(t_i, s)]\overline{\mathbf{C}}\dot{\sigma}(s)ds + \int_{t_i}^{t_{i+1}} [J(t_{i+1}, s) - J(t_{i,s})]\overline{\mathbf{C}}\dot{\boldsymbol{\sigma}}(s)ds \tag{A.16}$$

Assuming that the stress varies linearly over the time increment $\dot{\sigma} = \Delta\sigma/\Delta t$ and using a generalized midpoint rule $t_i \leqslant t^* \leqslant t_{i+1}$, the stress increment $\Delta\boldsymbol{\sigma} = \boldsymbol{\sigma}(t_{i+1}) - \boldsymbol{\sigma}(t_i)$ can be written as

$$\Delta\boldsymbol{\sigma} = \tilde{E}(t^*)\overline{\mathbf{C}}^{-1}\Delta\boldsymbol{\varepsilon} + \tilde{\boldsymbol{\sigma}}(t) \tag{A.17}$$

where

$$\tilde{E}(t^*) = \left(\frac{1}{\Delta t}\int_t^{t+\Delta t} J(t + \Delta t, s)ds\right)^{-1} \tag{A.18}$$

$$\tilde{\boldsymbol{\sigma}}(t_i) = -\tilde{E}(t^*)\left\{\overline{\mathbf{C}}^{-1}\Delta\boldsymbol{\varepsilon} - \int_0^{t_i} [J(t_{i+1}, s) - J(t_i, s)]\dot{\boldsymbol{\sigma}}(s)ds\right\} \tag{A.19}$$

The creep function $J(t, s)$ is defined in Eq. (A.20) by the Dirichlet series that is usually adopted in long-term creep simulations. Dirichlet series used in this study can be interpreted as a Kelvin chain with two elements, a spring complemented by a spring-damper system. The retardation time λ_i and the spring modulus E_i for the ith element of the Dirichlet chain are the required input.

$$J(t, s) = \sum_{i=0}^{1} \frac{1}{E_i(s)}\left(1 - e^{-\frac{t-s}{\lambda_i}}\right) \tag{A.20}$$

More information on the utilized creep model can be found in [14]

References

[1] Johannesson P, Tohlang SL. Lessons learned from Mohale. Int water power and dam constr 2007; July feature.

[2] Kovacevic N, Vaughan PR, Potts DM. A comparison between observed and predicted deformation of Winscar dam. In: Pande GN, Pietruszczak S, editors. Proceedings of the 8th international conference on numerical models in geomechanics. A.A. Balkema, Lisse, The Netherlands; 2002. p. 565–71.

[3] Lollino P, Cottechia F, Zdravkovic L. Numerical analysis and monitoring of Pappadai Dam. Can Geotech J 2005;42:1631–43.

[4] Kovacevic N, Vaughan PR, Potts DM. A comparison between observed and predicted deformations of an old dam during reservoir operation. In: Pande GN, Pietruszczak S, editors. Proceedings of the 9th international conference on numerical models in geomechanics. A. Balkema, Leiden, The Netherlands; 2004. p. 587–93.

[5] Prevost JH. Two surface versus multi-surface plasticity theories: a critical assessment. Int J Numer Anal Methods Geomech 1982;6:323–38.

[6] Dafalias YF. Bounding surface plasticity; mathematical foundation and hypoplasticity. ASCE J Eng Mech 1986;112:966–87.

[7] Kavvadas M, Amorosi A. A constitutive model for structured soils. Geotechnique 2000;50:263–73.

[8] Rouainia M, Muir Wood D. An implicit constitutive algorithm for finite strain Cam-clay elasto-plastic model. Mech Cohes-Frict Mater 2000;5:469–89.

[9] Aydingun O, Adalier K. Numerical analysis of seismically induced liquefaction in earth embankment foundations, Part I, benchmark model. Can Geotech J 2003;40(4):753–65.

[10] Elia G, Amorosi A, Chan AHC, Kavvadas M. Fully coupled dynamic analysis of an earth dam. Geotechnique 2010. doi:10.1680/geot.8.P.028.

[11] Uddin N. A dynamic analysis procedure for concrete-faced rockfill dams subjected to strong seismic excitation. Comput Struct 1999;72:409–21.

[12] Zhang G, Zhang JM. Numerical modelling of soil-structure interface of a concrete face rockfill dam. Comput Geotech 2009;36(5):762–72.

[13] Bayraktar A, Kartal ME. Linear and nonlinear response of concrete slab on CFR dam during earthquake. Soil Dyn Earthquake Eng 2010;30:990–1003.

[14] TNO DIANA. User's Manual R. 9.3; 2008.

[15] Feenstra PH, Rots JG, Arnesen A, Teigen JG, Høiseth KV. A 3D constitutive model for concrete based on a co-rotational concept. In: de Borst R, et al., editors. EURO-C 1998, computer modeling of concrete structures. Balkema, Rotterdam, The Netherlands; 1998. p. 13–22.

[16] Varadarajan A, Sharma KG, Venkatachalam K, Gupta AK. Testing and modeling two rockfill materials. J Geotech Geoenviron Eng 2003;129(3):206–18.

[17] Groen AE. Elastoplastic modelling of sand using a conventional model. Tech rep 03.21.0.31.34/35, Delft University of Technology; 1995.

[18] De Borst R, Van Den Boogard AH. Finite-element modelling of deformation and cracking in early-age concrete. J Eng Mech 1994;120(12):2519–34.

[19] Seo MW, Ha IS, Kim YS, Olson SM. Behavior of concrete-faced rockfill dams during initial impoundment. J Geotech Geoenviron Eng 2009;135(8):1070–81.

[20] Kramer SL. Geotechnical earthquake engineering. NJ: Prentice Hall; 1996.

[21] Seed HB, Wong RT, Idriss IM, Tokimatsu K. Moduli and damping factors for dynamic analysis of cohesionless soils. Rep no 84/14. EERC, Berkeley, California; 1984.

[22] Banerjee NG, Seed HB, Chan CK. Cyclic behavior of dense coarse grained sands in relation to seismic stability of dams. Rep no 79/13. EERC, Berkeley, California; 1979.

[23] Cao X, He Y, Xiong K. Confining pressure effect on dynamic response of high rockfill dam. Front Arch Civ Eng China 2010;4(1):116–26.

[24] Uesugi M, Kishida H, Uchikawa Y. Friction between dry sand and concrete under monotonic and repeated loading. Soils Found 1990;30(1):115–28.

[25] Vermeer PA, De Borst R. Non-associated plasticity for soils, concrete and rock. Heron 1984;29(3):3–64.

[26] Kutzner C. Earth and rockfill dams. Rotterdam: Balkema; 1997.

[27] Fell R, MacGregor P, Stapledon D, Bell G. Geotechnical engineering of dams. Rotterdam: Balkema; 2005.

[28] Cooke B. Progress in rockfill dams. Geotechnical Special Publication No. 1, Terzaghi Lectures, ASCE; 1986. p. 363–94.

[29] Gergely P, Lutz LA. Maximum crack width in reinforced concrete flexural members. In: Philleo RE, editor. Causes, mechanism and control of cracking in concrete, SP20. Detroit: American Concrete Institute; 1968. p. 87–117.

[30] ACI Committee 318. Building code requirements for structural concrete and commentary 2005. American Concrete Institute; 2004.

[31] Pinto NLP, Filho PLM, Maurer E. Foz do Areia Dam-design, construction, and behaviour. In: Cooke JB, Sherard JL, editors. Proceedings of the symposium on concrete face rockfill dams: design, construction and performance. New York: ASCE; 1986. p. 173–91.

[32] Askan-Gundogan A, Ozturk N. Seismic hazard study for Cokal Dam. Earthquake Engineering Research Center, METU, Ankara; 2010.

[33] Gazetas G. Seismic response of earth dams: some recent developments. Soil Dyn Earthquake Eng 1987;6(1):2–47.